Materials Characterization 205 (2023) 113372

Contents lists available at ScienceDirect

Materials Characterization

journal homepage: www.elsevier.com/locate/matchar

Tensile behaviors and hetero-deformation-induced hardening mechanisms in medium entropy alloys with dual gradients of grain size and coherent nanoprecipitate

Zihan Zhang [a,b], Xiaolei Wu [a,b], Fuping Yuan [a,b,*]

[a] State Key Laboratory of Nonlinear Mechanics, Institute of Mechanics, Chinese Academy of Science, 15 Beisihuan West Road, Beijing 100190, China
[b] School of Engineering Science, University of Chinese Academy of Sciences, 19A Yuquan road, Beijing 100049, China

ARTICLE INFO

Keywords:
High/medium entropy alloys
Heterogeneous structures
Gradient structure
Precipitation hardening
Strengthening
Ductility

ABSTRACT

Heterogeneous structures with dual gradients of grain size and coherent $L1_2$ nanoprecipitation have been designed and fabricated in a $Co_{34.46}Cr_{32.12}Ni_{27.42}Al_3Ti_3$ medium entropy alloy. These heterogeneous structures with dual gradients show improved tensile properties over both the single grain-size gradient structure and the coarse grained structures with homogeneously distributed $L1_2$ nanoprecipitates. Hetero-deformation-induced hardening rate was observed to be higher and the strain hardening capacities at each depth were also found to be higher in the structures with dual gradients, as compared to the single grain-size gradient structure. Deformation twins and stacking faults were observed at both the topmost and center layers, while deformation bands at two directions were only found at the topmost layer after tensile deformation in the single grain-size gradient structure. Strong interactions between defects and coherent $L1_2$ nanoprecipitates can be observed at all depths after tensile deformation in the structures with dual gradients, resulting in strong precipitation hardening. While, stronger precipitation hardening was achieved at the topmost layer due to the higher volume fraction and smaller spacing of coherent $L1_2$ nanoprecipitates, which could delay the early necking trend at the topmost layer for better tensile ductility in the structures with dual gradients.

1. Introduction

Metals and alloys with both high strength and large ductility are the perpetual pursuit for the communities of materials science and mechanical engineering [1–11]. While, it is well known that strength and ductility are mutually exclusive, and an elevation in strength is always accompanied with a loss in tensile ductility in metal and alloys with homogeneous structures [3,4,8,12–16].

Precipitates, especially coherent nanoprecipitates, can be an effective way for improving yield strength while maintaining appreciable tensile ductility in metal and alloys due to the shearing or bypassing precipitation strengthening/hardening mechanisms [17–25]. However, the enhancement in strength by nanoprecipitates in coarse grains (CGs) is limited, and the ductility by precipitation in ultrafine grains (UFGs) is inevitable sacrificed [21,23–25]. Moreover, the increase of volume fraction of nanoprecipitates can give rise to an elevation in strength, while could be accompanied with a loss of tensile ductility [23–25]. The strength-ductility trade-off has not been fully resolved although excellent synergy of strength and ductility can be achieved in the metals and alloys with homogeneous structures with coherent nanoprecipitates. In the previous research [24], superior synergy of strength and ductility was achieved in a Co-Cr-Ni-based medium-entropy alloy (MEA) with dual heterogeneous structures (heterogeneous grain structure and coherent nanoprecipitates). Thus, combination of heterogeneous structures and coherent nanoprecipitates is an effective strategy to evade the strength-ductility dilemma.

In last decade, gradient structures have been shown to be another effective strategy to evade the strength-ductility dilemma [26–30]. In the gradient structures, strain gradients and geometrically necessary dislocations (GNDs) can be generated at layer boundaries due to the strain/stress partitioning during tensile loading, resulting in extra hetero-deformation-induced (HDI) hardening for superior tensile properties [16,31–33]. The strategies of gradient structures and nanoprecipitates have also been applied to high-entropy alloys (HEAs) and

* Corresponding author at: State Key Laboratory of Nonlinear Mechanics, Institute of Mechanics, Chinese Academy of Science, 15 Beisihuan West Road, Beijing 100190, China.
E-mail addresses: zhangzihan@imech.ac.cn (Z. Zhang), xlwu@imech.ac.cn (X. Wu), fpyuan@lnm.imech.ac.cn (F. Yuan).

https://doi.org/10.1016/j.matchar.2023.113372
Received 29 March 2023; Received in revised form 6 September 2023; Accepted 2 October 2023
Available online 5 October 2023

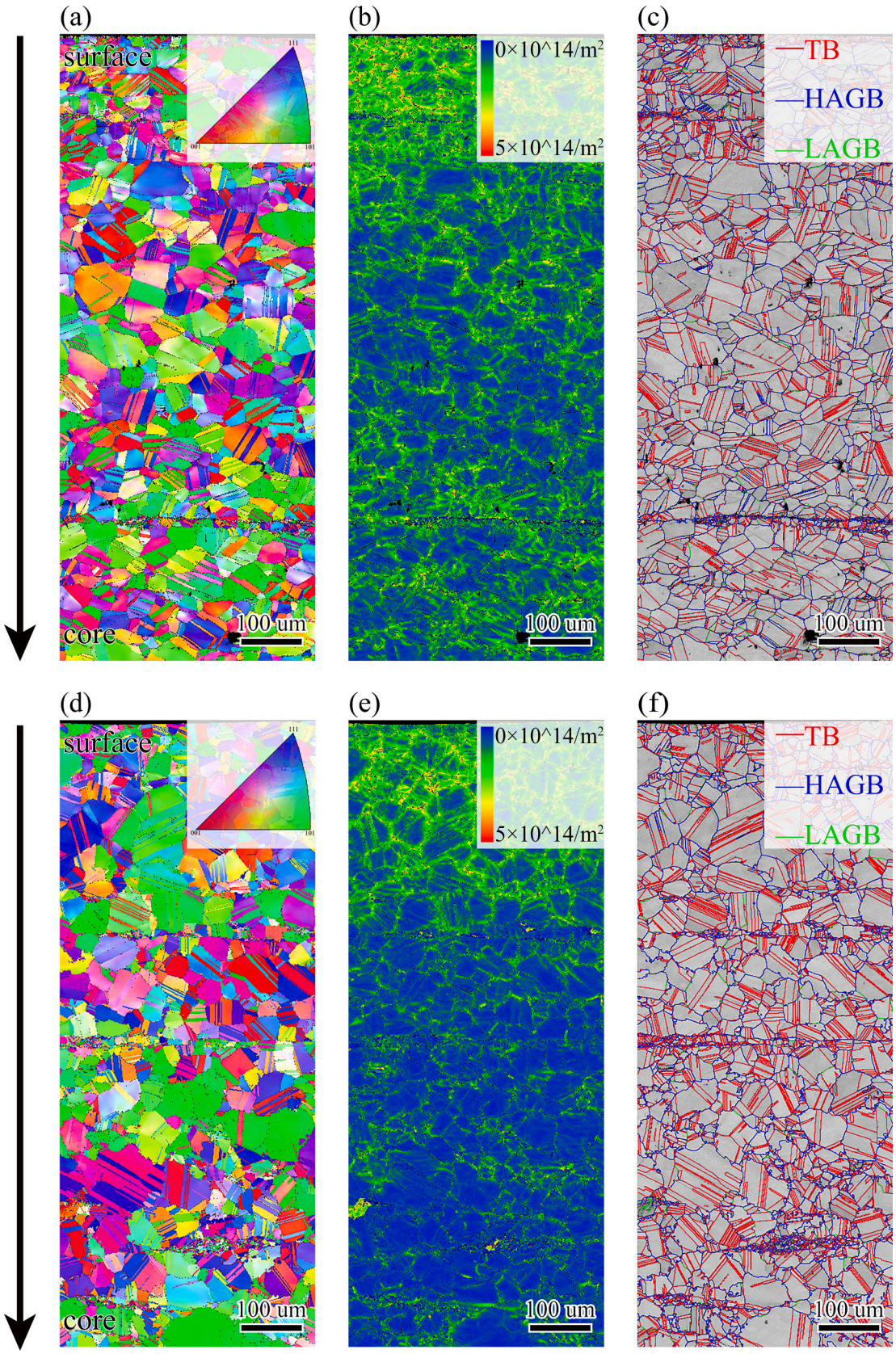

Fig. 1. Microstructures characterizations along the depth for the SMGT sample and the SMGT-Aged-30 m sample before tensile testing. The SMGT sample: (a) IPF image; (b) KAM map; (c) Image with various boundaries. The SMGT-Aged-30 m sample: (d) IPF image; (e) KAM map; (f) Image with various boundaries.

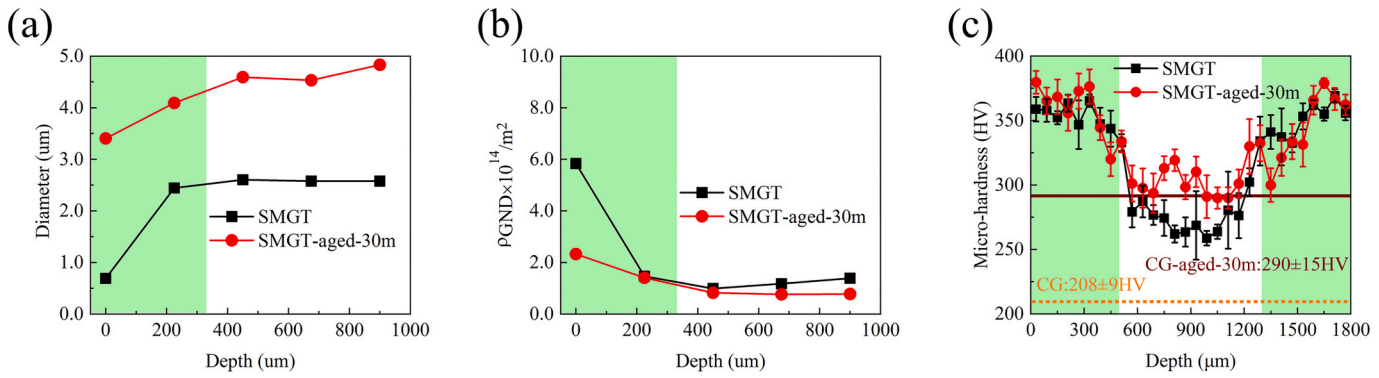

Fig. 2. (a) Grain size distributions along the depth for the SMGT sample and the SMGT-Aged-30 m sample. (b) Distributions of GND density along the depth the SMGT sample and the SMGT-Aged-30 m sample. (c) Micro-hardness distributions along the depth the SMGT sample and the SMGT-Aged-30 m sample.

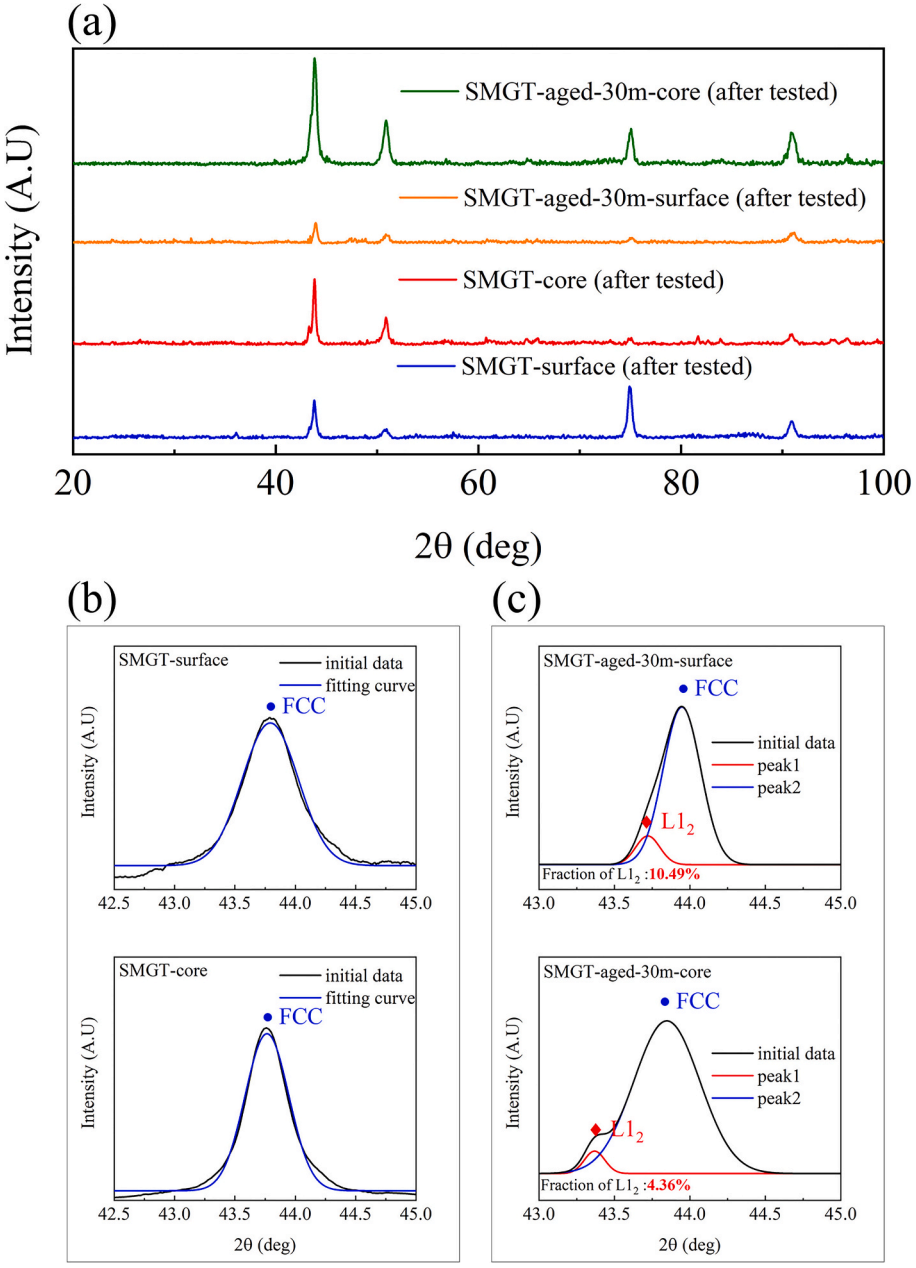

Fig. 3. (a) XRD spectra for the SMGT sample and the SMGT-aged-30 m sample at both the topmost and center layers. (b) The close-up views of (111) peaks for the SMGT sample at both the topmost and center layers. (c) The close-up views of (111) peaks for the SMGT-aged-30 m sample at both the topmost and center layers.

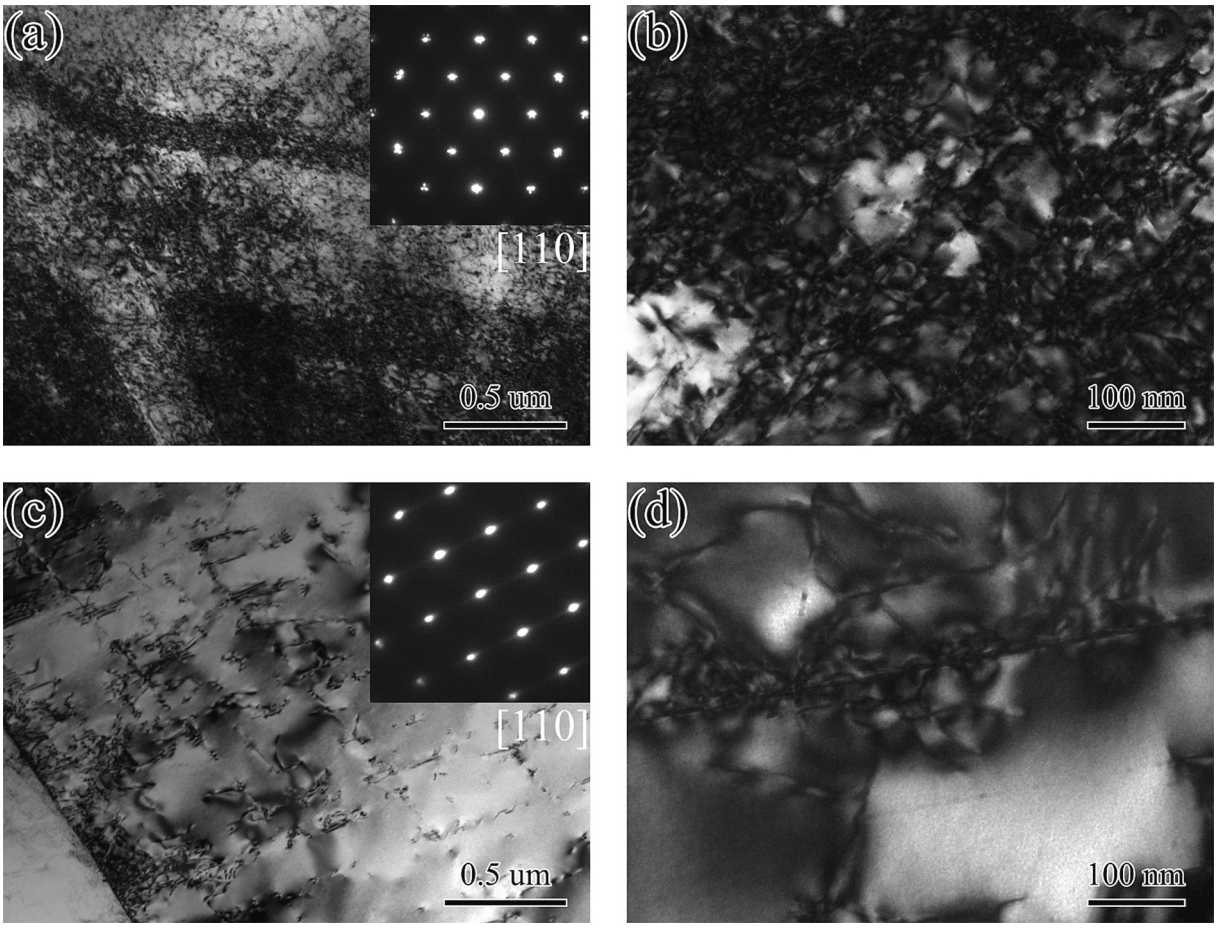

Fig. 4. (a) (b) Bright-field TEM images at the topmost layer for the SMGT sample. (c) (d) Bright-field TEM images at the center layer for the SMGT sample.

MEAs for achieving extraordinary mechanical properties [24,26,29]. HEAs and MEAs have drawn extensive attentions recently as a new class of materials due to their outstanding mechanical properties [7,10,13,15,18,23]. Particularly, extensive research interests have been focused on the FeCrMnCoNi HEA [25,34–36], the CoCrNi MEA [22–24,29,37–42] and their based-HEAs/MEAs due to their extraordinary mechanical properties under room temperature and even better mechanical properties under cryogenic temperature [4,21,43].

It is reasonable to propose that even better tensile properties can be obtained by deploying dual gradients of grain size and volume fraction of coherent nanoprecipitates in HEAs/MEAs due to both the benefits from these two microstructures and the possible extra coupling effect. Moreover, the topmost layer in the gradient structures is generally the "brittle" layer with high propensity for plastic deformation localization, thus certain extra hardening mechanism should be induced for suppressing the plastic flow instability in the topmost layer. In the "pure" gradient structures (with only grain size gradients), the mechanically-induced grain growth at the topmost layer and the HDI extra hardening by strain gradients and GNDs have been found to play important roles on delaying the strain localization and sustaining large uniform elongation in the topmost layer [31–33,44,45].

It can be imaged that stronger precipitating hardening can be induced in the topmost layer due to the higher volume fraction of nanoprecipitates, thus the reduced strain hardening capacity by the nanostructured topmost layer can be compensated due to this stronger precipitating hardening. As a result, the early plastic flow instability in the topmost layer can be prevented, and better tensile ductility could be achieved in the structures with dual gradients. However, such structures with dual gradients of grain size and volume fraction of coherent nanoprecipitation have been rarely built in metals and alloys, especially in HEAs/MEAs [17–25,46]. Moreover, the detailed strengthening/strain hardening mechanisms for such structures with dual gradients are still unclear. In this perspective, the structures with dual gradients were designed and fabricated in a Co-Cr-Ni-based MEA ($Co_{34.46}Cr_{32.12}Ni_{27.42}Al_3Ti_3$, in at.%) by surface mechanical grinding treatment (SMGT) and aging treatment. The chemical composition of our materials is the same as that for a Co-Cr-Ni-based MEA in the previous research [24], while the microstructures (structures with dual gradients) in the present study are dramatically different from those (bi-modal grain structure and coherent nanoprecipitates) in the previous research [24]. Thus, the tensile behaviors and the corresponding hardening mechanisms should be different and need to be revealed. In this regard, the tensile behaviors and the corresponding deformation mechanisms for such structures with dual gradients have been studied and compared with those for structures with single gradient and for structures with homogeneous CGs and homogeneously distributed coherent nanoprecipitates.

2. Materials and experimental techniques

The materials were prepared by induction melting furnace. The Co-Cr-Ni-based MEA ($Co_{34.46}Cr_{32.12}Ni_{27.42}Al_3Ti_3$, in at.%) was prepared by melting for several times with an argon atmosphere. The homogenized ingots were heated to 1423 K and then hot-forged into 18 mm thick plates. The hot-forged plates were annealed at 1473 K under vacuum environment for 2 h, followed by water quenching. The thickness of the annealed plates was reduced from about 18 mm to about 1.8 mm by a multi-pass cold rolling process. The cold rolled plates were annealed again at 1273 K for 1 h followed by water quenching, and the samples under this conditions are named as the CG samples. Some CG

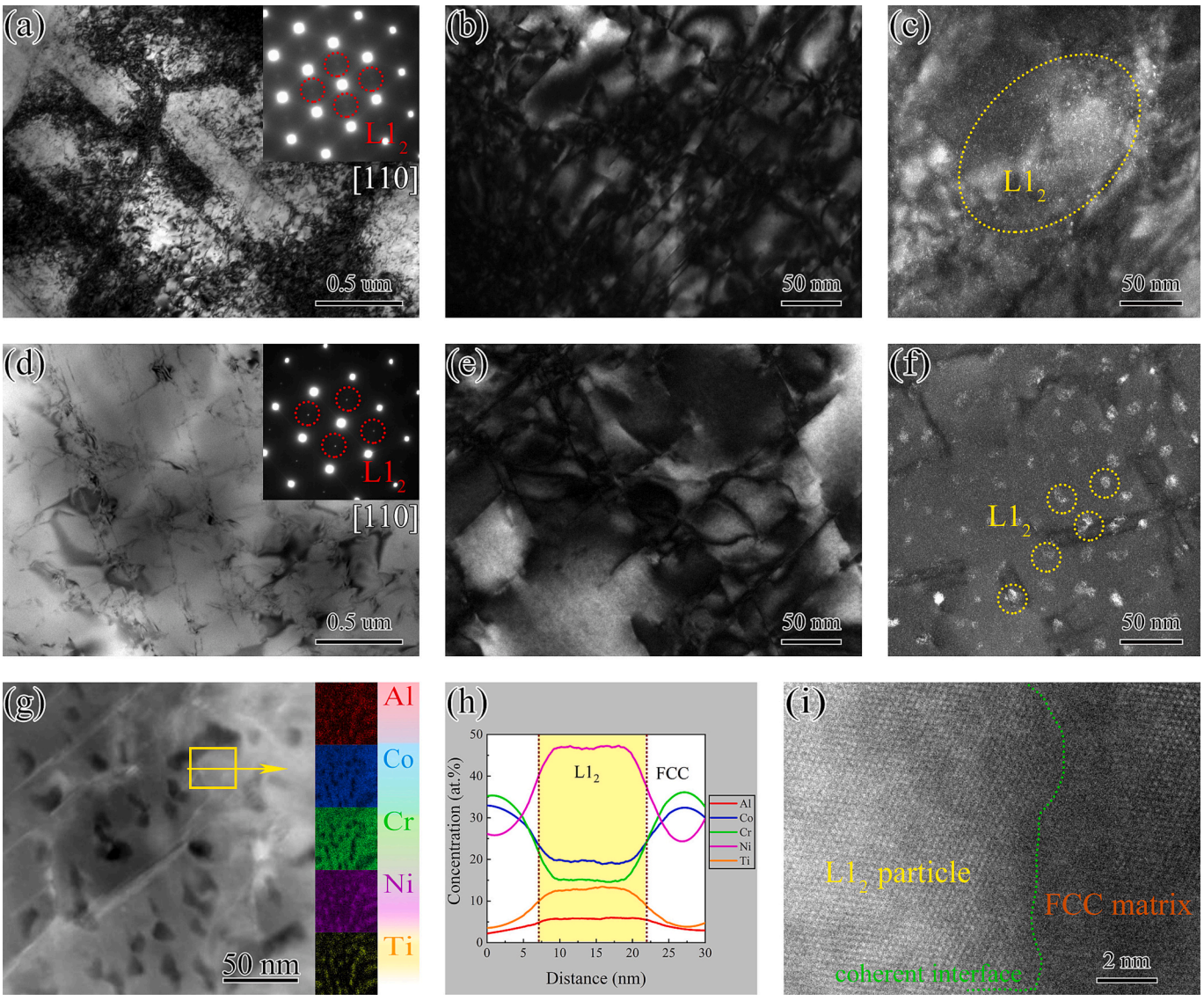

Fig. 5. (a) (b) Bright-field TEM images at the topmost layer for the SMGT-aged-30 m sample. (c) Dark-field TEM image at the topmost layer for the SMGT-aged-30 m sample. (d) (e) Bright-field TEM images at the center layer for the SMGT-aged-30 m sample. (f) Dark-field TEM image at the center layer for the SMGT-aged-30 m sample. (g) EDS mapping for an area with numerous $L1_2$ precipitates. (h) Element distributions along the mark line in (g). (i) HRTEM image showing the coherent interface between a $L1_2$ precipitate and FCC matrix.

samples were then processed by SMGT, in which both sides of samples were impacted by 4 mm diameter steel balls with an impact velocity of about 20 m/s and a processing time of 15 min for each side. The samples after SMGT are named as the SMGT samples. More details about SMGT can be found elsewhere [30,47–50]. Some CG samples were aged at 973 K for various times (10, 20, 30, 60, 120, 240 min), and these samples are called as the CG-Aged samples (CG-aged-10 m, CG-aged-20 m, CG-aged-30 m, CG-aged-60 m, CG-aged-120 m, CG-aged-240 m). Some SMGT samples were also aged at 973 K for various times (10, 20, 30, 60, 120, 240 min), and these samples are named as the SMGT-Aged samples (SMGT-aged-10 m, SMGT-aged-20 m, SMGT-aged-30 m, SMGT-aged-60 m, SMGT-aged-120 m, SMGT-aged-240 m). The tensile properties and the microstructural mechanisms for the SMGT-Aged samples were then investigated and compared with those for the SMGT sample and the CG-Aged samples.

The specimens for quasi-static tensile and load-unload-reload (LUR) experiments have a dog-bone shape with a thickness of about 1.8 mm, a gauge length of 10 mm and a gauge width of 2.5 mm. The tensile and LUR experiments were conducted at a strain rate of 5 × 10–4 /s and under room temperature, and the displacement in these tests was carefully controlled and measured by an extensometer. Three repeated experiments were conducted for each sample, and the error bars were provided. The details for LUR experiments can be referred to our previous paper [16,31–33]. The micro-hardness distributions for the SMGT samples and the SMGT-Aged samples prior to and after tensile testing were characterized using a Vickers diamond indenter with a load of 100 g for 15 s dwell time. Ten groups of indentations for each depth were applied, and the average value was provided with an error bar. Energy disperse spectroscopy (EDS), X-ray diffraction (XRD), electron backscattered diffraction (EBSD), transmission electron microscopy (TEM) and high-resolution TEM (HRTEM) were used to reveal the microstructures prior to and after tensile tests. The detailed procedures for these techniques can be found in previous research [22,43,46].

3. Results and discussions

The microstructure characterizations for the SMGT sample and one selected SMGT-aged sample (SMGT-aged-30 m) prior to tensile tests are

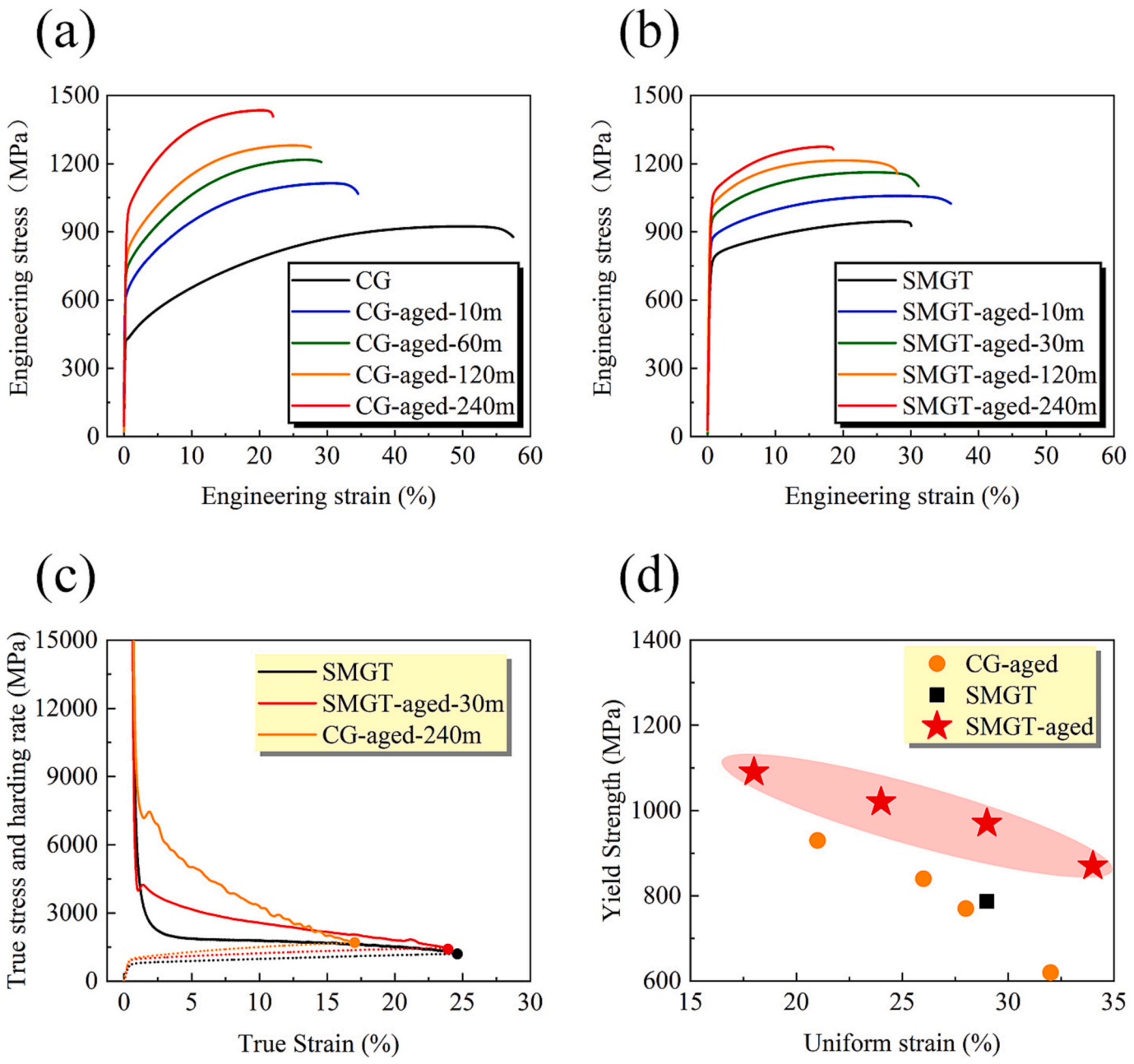

Fig. 6. Tensile properties for various samples. (a) Engineering stress-strain curves for the CG sample and the CG-Aged samples. (b) Engineering stress-strain curves for the SMGT sample and the SMGT-aged samples. (c) The curves of hardening rate and true stress as a function of true strain for the SMGT sample, the SMGT-aged-30 m sample and the CG-Aged-240 m sample. (d) Yield strength vs. uniform elongation for all samples tested in the present study.

displayed in Figs.1 and 2. The images of inverse pole figure (IPF) for these two samples are given in Figs.1a and 1d, the corresponding kernel average misorientation (KAM) maps are shown in Figs.1b and 1e, and the corresponding images with high-angle grain boundaries (HAGBs), low-angle grain boundaries (LAGBs) and $\sum 3$ twin boundaries (TBs) are displayed in Figs.1c and 1f. Then, the distributions of grain size and GND density along the depth for these two samples are given in Figs. 2a-2b. The GND density is calculated from the KAM value based on the method from the previous research [22,31–33,43]. It is interesting to note that both samples display gradients for grain size and GND density along the depth. The gradient of GND density can reflect the gradient for the sub-structures, such as dislocation cells, dislocation walls, and LAGBs. Moreover, it is shown that the magnitudes of both grain size and GND density gradients are weaker for the SMGT-aged sample, indicating dynamic recovery and grain growth after aging treatment. The micro-hardness distributions for these two samples are given in Fig. 2c.

The XRD spectra for the SMGT sample and the SMGT-aged-30 m sample at both the topmost and center layers are given in Fig. 3a. As indicted in the close-up views (Fig. 3c), the (111) peaks for the SMGT-aged-30 m sample at both the topmost and center layers are asymmetric due to the superimposition of peaks for the FCC phase and the coherent $L1_2$ phase. Thus Gauss function fitting has been utilized to obtain the individual peaks for the FCC phase and the coherent $L1_2$ phase, and then the relative volume fractions of the $L1_2$ precipitates in the FCC matrix at both the topmost and center layers are estimated to be 14.6% for the topmost layer and 7.7% for the center layer by the integrated areas of the separated (111) peaks. While, the (111) peaks for the SMGT sample at both the topmost and center layers (Fig. 3b) are both shown to be symmetric, indicating a single FCC phase without L12 precipitates for the SMGT sample.

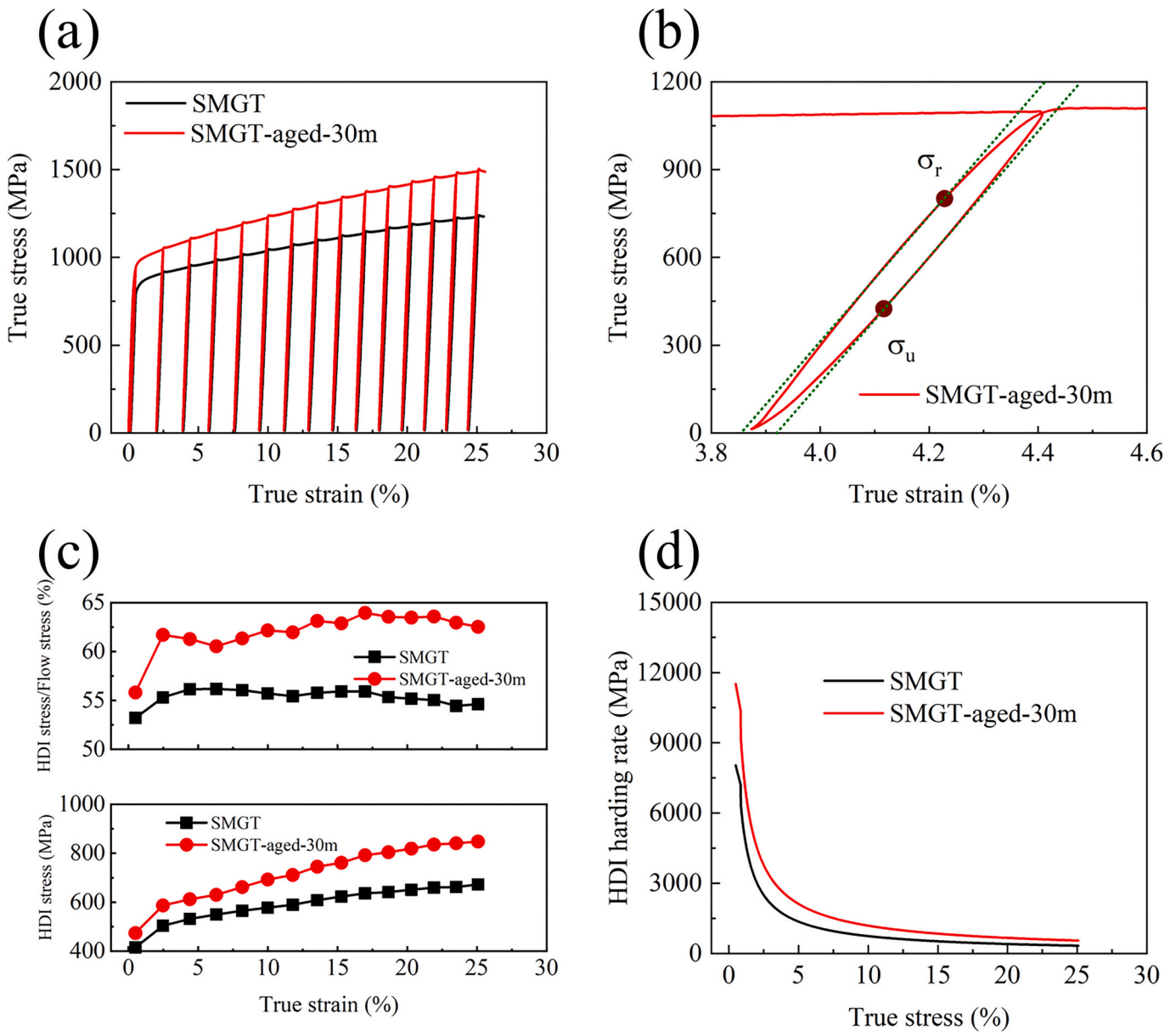

Fig. 7. HDI hardening for the SMGT sample and the SMGT-aged-30 m sample. (a) True stress-true strain curves of LUR tests. (b) Close-up views of typical hysteresis loops. (c) HDI stress, and ratio of HDI stress and flow stress as a function of true strain. (d) HDI hardening rate vs. true strain.

The characterizations for the microstructures and the $L1_2$ precipitates in the SMGT sample and the SMGT-aged-30 m sample at both the topmost and center layers are further revealed and confirmed by TEM and HRTEM observations, as shown in Figs. 4 and 5. Bright-field TEM images at the topmost layer for the SMGT sample are shown in Figs. 4a and 4b, while bright-field TEM images at the center layer for the SMGT sample are displayed in Figs. 4c and 4d. High density of dislocations can be observed at the topmost layer, and numerous substructures (dislocation cells and dislocation walls by planar slip) are also found to be formed in the grain interiors. As a contrast, the dislocation density is found to be much lower at the center layer. These observations are consistent with the results in Fig. 1b.

Bright-field TEM images at the topmost layer for the SMGT-aged-30 m sample are shown in Figs. 5a and 5b, while bright-field TEM images at the center layer for the SMGT-aged-30 m sample are displayed in Figs. 5d and 5e. Similar to the SMGT sample, the dislocation density is much higher at the topmost layer, as compared to the center layer in the SMGT-aged-30 m sample. The selected diffraction electron patterns (SAEDs) in the insets of Figs. 5a and 5d indicate the co-existence of FCC matrix and $L1_2$ precipitates, while the $L1_2$ precipitates can't be observed in these bright-field images. In this regard, the dark-field TEM images at the topmost layer and at the center layer are displayed in Figs. 5c and 5f, respectively. In these two figures, the brighter particles are $L1_2$ precipitates. The average size of $L1_2$ precipitates at the topmost layer is observed to be much smaller than that at the center layer (0.84 nm vs. 7.8 nm), while the volume fraction of L12 precipitates at the topmost layer is found to be much higher at the topmost layer as compared to that at the center layer (12.0% vs. 7.1%). EDS mapping for an area with numerous L12 precipitates is given in Fig. 5 g, and the element distributions along the mark line in Fig. 5 g is shown in Fig. 5 h. It is indicated that Ni and Ti elements are highly enriched and Al element is slightly enriched, while Co and Cr elements are deprived in the $L1_2$ precipitates. HRTEM image with a $L1_2$ precipitate is displayed in Fig. 5i, in which the coherent interface between the $L1_2$ precipitate and FCC matrix can be clearly identified. The gradients for GND density are more obvious than those for grain size for both SMGT and SMGT-aged-30 m samples. The

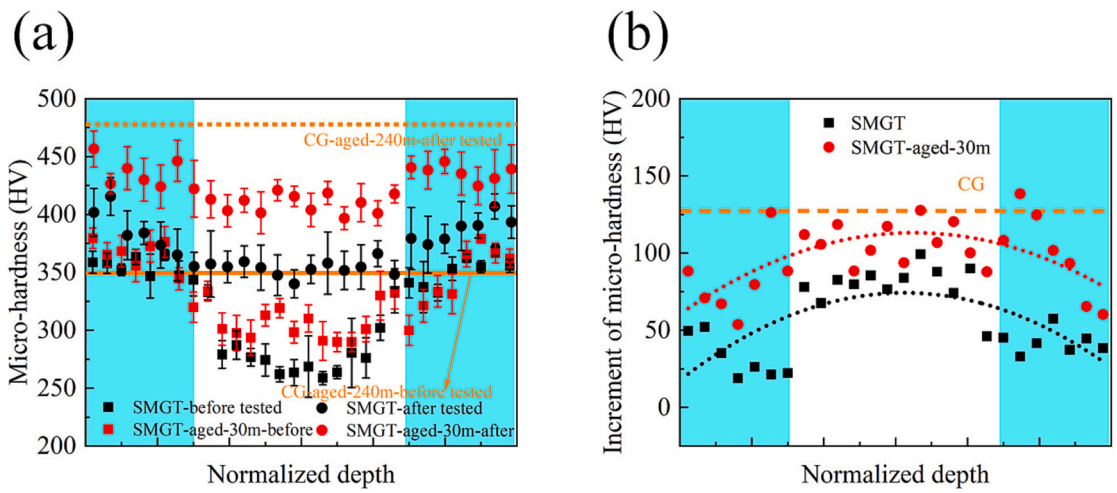

Fig. 8. (a) Micro-hardness distributions along the depth for the SMGT sample and the SMGT-aged-30 m sample prior to and after tensile deformation. The corresponding micro-hardness for the CG-Aged-240 m sample prior to and after tensile deformation are also given by an orange solid line and an orange dash line, respectively. (b) Distributions of hardness increment along the depth after tensile deformation for the SMGT sample and the SMGT-aged-30 m sample. The corresponding micro-hardness increment for the CG-Aged-240 m sample is also given by an orange dash line.

grain size was calculated based on the HAGBs. While, the gradient of GND density can reflect a gradient on the density of substructures (such as dislocation walls, dislocation cells, LAGBs). Thus, an obvious gradient in various boundaries was induced after SMGT, especially at the surface layer. As shown in Figs. 1–5, the microstructure in the SMGT sample shows a single gradient on defect density (densities of LAGBs and HAGBs), while the dual gradients (defect density and volume fraction of $L1_2$ precipitates) along the depth are observed in the SMGT-aged-30 m sample. The formation of phase volume fraction ($L1_2$ nanoprecipitates) along the depth should be due to the graded magnitude for plastic deformation during SMGT and the subsequent aging. The stored plastic deformation energy should show a gradient distribution along the depth after SMGT, thus the topmost layer with highest energy state and highest defects (short-circuit diffusion) should have the greatest potential for formation of $L1_2$ phases during the subsequent aging, resulting in a phase gradient along the depth.

The tensile properties for various samples are displayed in Fig. 6. The engineering stress-strain curves for the CG sample and the CG-Aged samples are shown in Fig. 6a, while the engineering stress-strain curves for the SMGT sample and the SMGT-aged samples are given in Fig. 6b. The curves of hardening rate and true stress as a function of true strain for the SMGT sample, one selected SMGT-aged sample (SMGT-aged-30 m) and one selected CG-Aged sample (CG-Aged-240 m) are displayed in Fig. 6c. Then, the yield strength is plotted as a function of the uniform elongation for all samples tested in the present study in Fig. 6d. It is observed that the yield strengths of the CG-Aged samples are higher while the uniform elongations are lower than those of the CG sample. Moreover, the yield strength is found to increase with aging time, while the uniform elongation is observed to decrease with aging time for the CG-Aged samples. These observations indicate that the precipitation on the CG sample can induce a good combination of strength and ductility, but the yield strength-tensile ductility trade-off still exists. However, the yield strength and the uniform elongation are observed to be simultaneously elevated for the SMGT-aged samples with short aging time, as compared to those of the SMGT sample. With further increasing aging time, and the yield strength of the SMGT-aged samples can be further improved, while the uniform elongation is observed to be reduced. The synergy of yield strength and tensile ductility of the SMGT-aged samples is observed to be better than those for the SMAT sample, the CG sample and the CG-Aged samples. These observations indicate that the structures with dual gradients have advantages on tensile properties not only over the structures with single gradient, but also over the structures with CGs and homogeneously distributed coherent nanoprecipitates. It is clearly observed (Fig. 6c) that the hardening rate is higher in the SMGT-aged-30 m sample as compared to the SMGT sample, while are lower than that for the CG-Aged-240 m sample. While, the hardening rate in the CG-Aged-240 m sample decreases more quickly than that for the SMGT-aged-30 m sample. Thus, the high hardening capacity sustaining in a longer tensile strain range could be one of origins for the better tensile properties in the structures with dual gradients.

As indicated in Fig. 6, the SMGT-aged-30 m sample shows a much higher yield strength and a higher hardening rate, while a similar uniform elongation, as compared to the SMGT sample. In order to understand the possible deformation mechanisms for the improved tensile properties in the structures with dual gradients, the HDI hardening for these two samples are characterized by LUR tests. It well known that HDI extra hardening can be induced in the heterogeneous structures, resulting in excellent mechanical properties [16,22,31–33]. Higher HDI hardening might be induced with increasing heterogeneity (e.g., dual gradients), resulting in even better tensile properties. Thus, the true stress-true strain curves of LUR tests for these two samples are shown in Fig. 7a, the close-up views of typical hysteresis loops for these two curves are displayed in Fig. 7b. Based on the hysteresis loops and the method proposed in our previous paper [22,32,43], the back stress (HDI stress) can be calculated. The HDI stress, and the ratio of HDI stress and flow stress are plotted as a function of true strain for these two samples in Fig. 7c. The HDI hardening rate is plotted as a function of true strain for these two samples in Fig. 7d. It is clearly observed that the HDI stress, the ratio of HDI stress and flow stress and the HDI hardening rate are higher in the structures with dual gradients as compared to the structures with single gradient. In the previous research [16,31], HDI extra hardening has been found to play a crucial role on the tensile behaviors and properties for structures with single grain-size gradient. However, it is obvious that structures with dual gradients can induce even higher HDI hardening rate, and this higher HDI hardening rate can provide additional hardening origin for the nanostructured topmost layer and prevent the early plastic flow instability in the topmost layer for better tensile ductility. Thus, the higher HDI extra hardening sustaining in a long tensile strain range could be one of origins for the better tensile properties in the structures with dual gradients.

It is shown that the SMGT-aged-30 m sample shows stronger overall hardening and HDI hardening than the SMGT sample. In order to understand how each depth contributes to the overall hardening, the

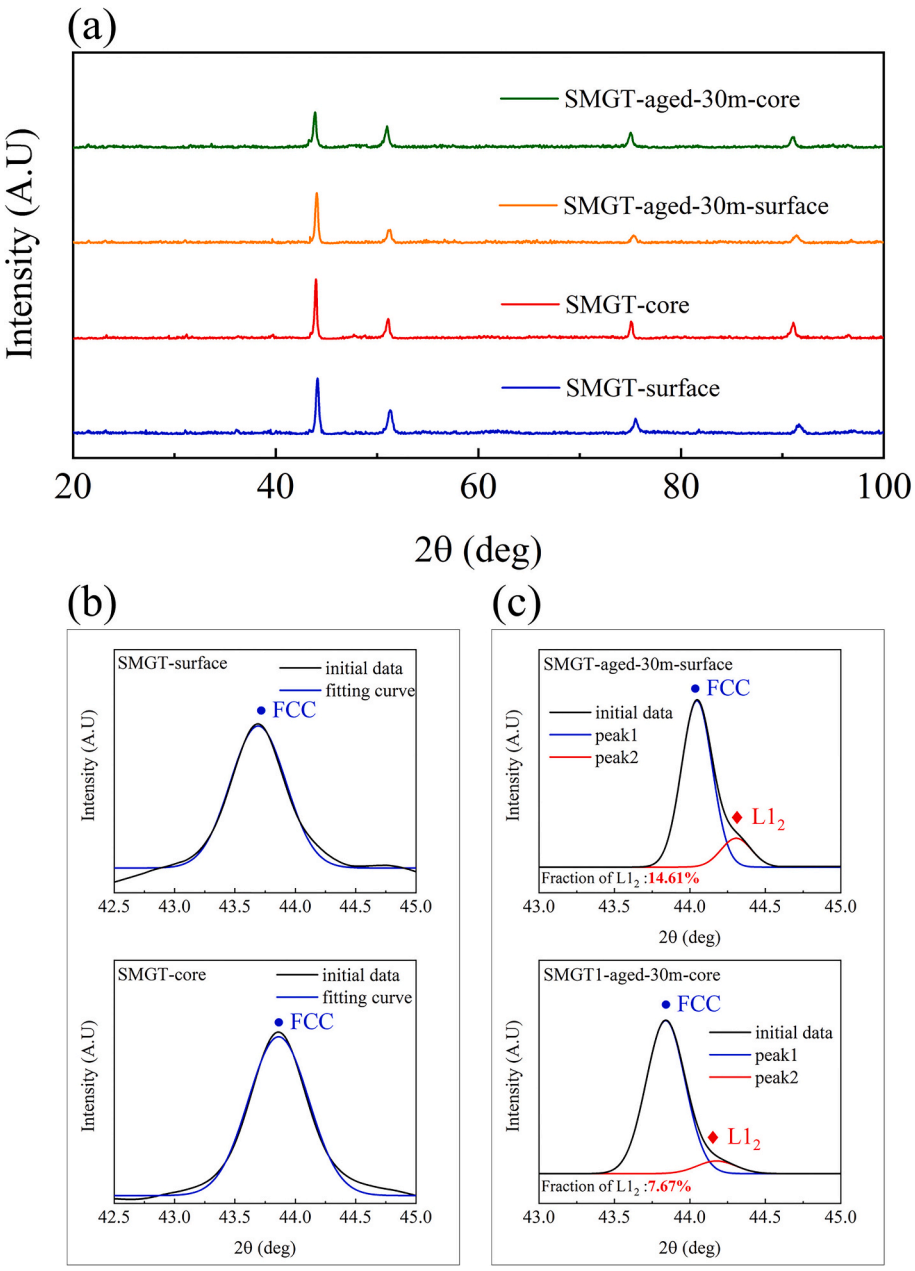

Fig. 9. (a) XRD spectra for the SMGT sample and the SMGT-aged-30 m sample at both the topmost and center layers after tensile deformation. (b) The close-up views of (111) peaks for the SMGT sample at both the topmost and center layers. (c) The close-up views of (111) peaks for the SMGT-aged-30 m sample at both the topmost and center layers.

micro-hardness distributions along the depth prior to and after tensile deformation for various samples are measured and displayed in Fig. 8a. The corresponding distributions of hardness increment after tensile deformation are shown in Fig. 8b. In general, the hardness increment can be considered as the hardening capacity of materials after plastic deformation. It is indicated that the hardening capacity is higher at the center layer and lower at the surface layer for both the SMGT sample and the SMGT-aged-30 m sample. Moreover, the hardening capacity of the SMGT-aged-30 m sample at each depth is higher than that of the SMGT sample. The average hardness increment of the SMGT-aged-30 m sample is calculated to be about 98 HV, which is higher than that of the SMGT sample (about 57 HV), while lower than that of the CG-Aged-240 m sample (about 126 HV). These findings are consistent with the results in Fig. 6c.

The XRD spectra for the SMGT sample and the SMGT-aged-30 m sample at both the topmost and center layers after quasi-static tensile testing are given in Fig. 9a. The close-up views of the (111) peaks at both the topmost and center layers for the SMGT sample and the SMGT-aged-30 m sample are shown in Fig. 9b and c. Single FCC phase is still observed for the SMGT sample after tensile deformation, indicating no phase transformation during quasi-static tensile loading. The relative volume fractions of the $L1_2$ precipitates in the FCC matrix at the topmost layer and at the center layer for the SMGT-aged-30 m sample are calculated to be 10.5% and 4.4%, respectively. These two values are lower than those prior to tensile testing, which might be due to the shearing mechanisms of $L1_2$ precipitates by dislocations as indicated later.

The microstructures for the SMGT sample at both the topmost and the center layers are also characterized by TEM and HRTEM images, as shown in Fig. 10. In previous research [22,43,51–53], it has been indicated that stacking fault energy (SFE) can be locally varied in HEAs/MEAs due to the inhomogeneous element distributions at the atomic

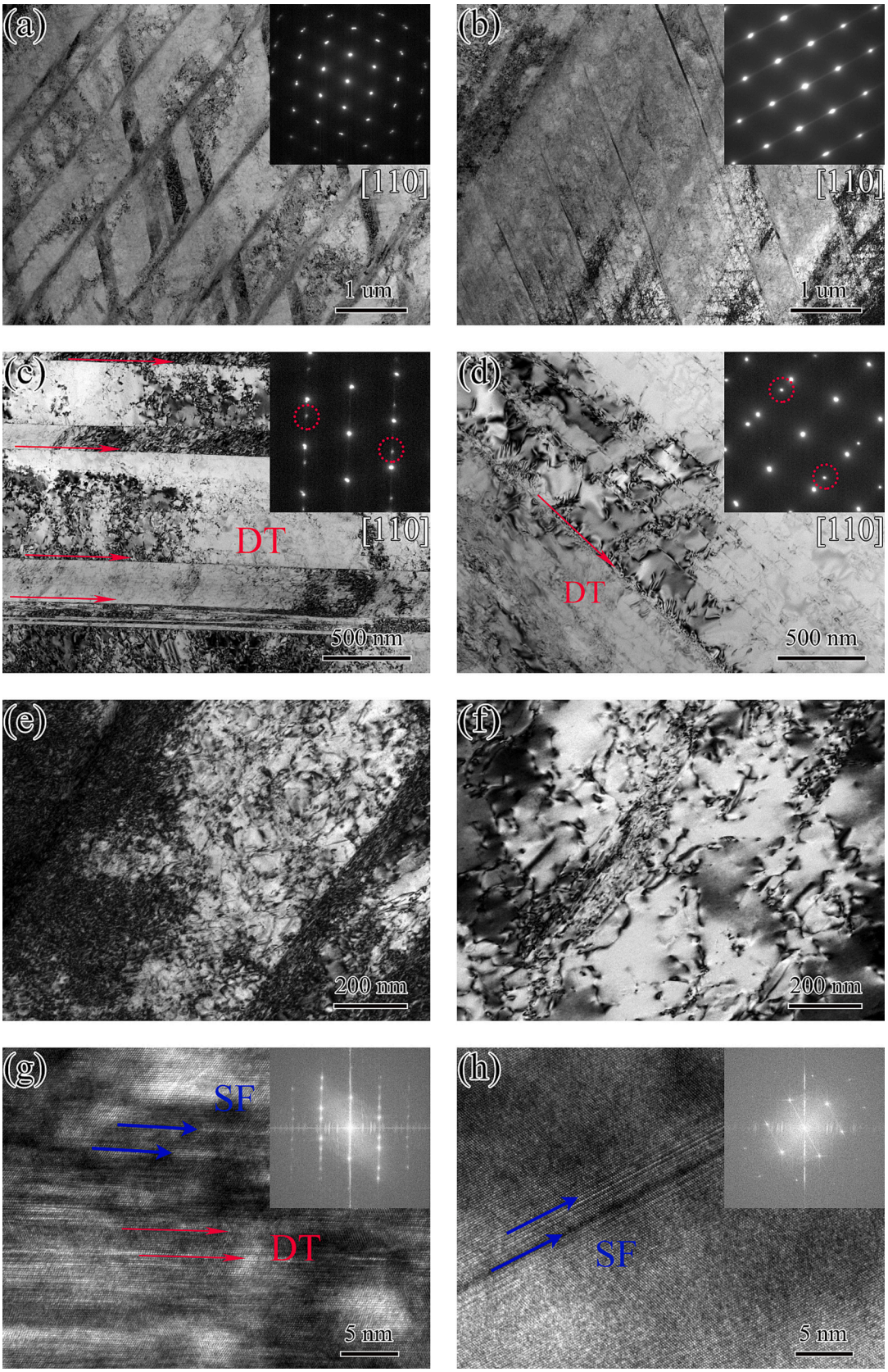

Fig. 10. TEM and HRTEM images for the SMGT sample. (a) (c) (e) Bright-field TEM images at the topmost layer. (b) (d) (f) Bright-field TEM images at the center layer. (g) HRTEM image at the topmost layer. (h) HRTEM image at the center layer.

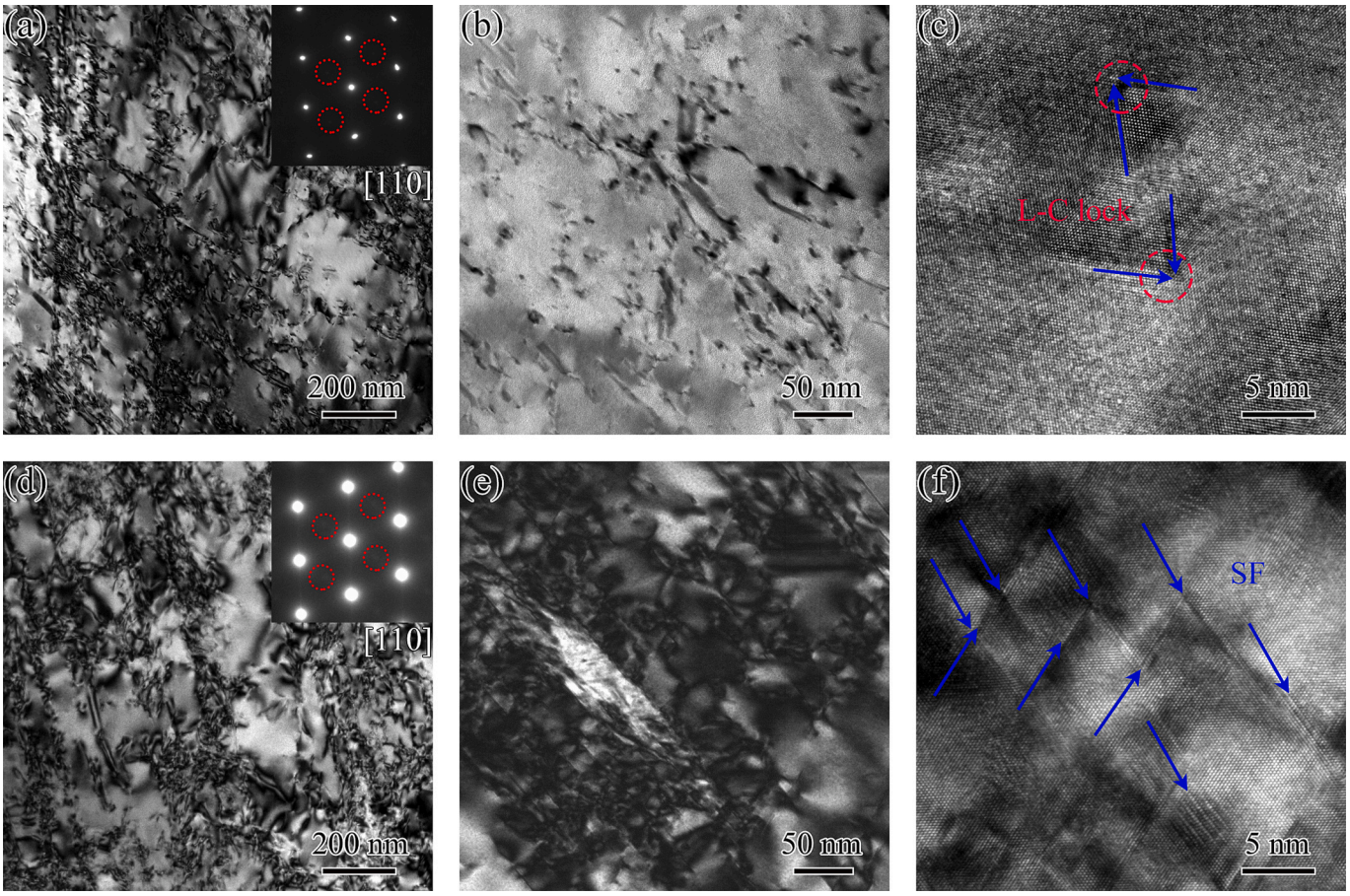

Fig. 11. TEM and HRTEM images for the SMGT-aged-30 m sample. (a) (b) Bright-field TEM images at the topmost layer. (c) (d) Bright-field TEM images at the center layer. (c) HRTEM image at the topmost layer. (f) HRTEM image at the center layer.

level. Due to this inhomogeneous distributed SFE, the deformation mechanisms can be dramatically different from point to point. It is interesting to note that planar slip, deformation twins (DTs), stacking faults (SFs) and non-planar dislocations are all observed in the SMGT sample at both the topmost and center layers. Multiple deformation mechanisms are observed due to the locally varied SFE in this MEA. Deformation bands at two directions are formed due to extensive planar slips at two slip systems at the topmost layer (Fig. 10a), while numerous planar slips are observed without formation of deformation band at the center layer (Fig. 10b). The density of DTs and SFs is observed to be higher at the topmost layer than that at the center layer (Fig. 10c, d, g, h). The observed higher density of defects at the topmost layer after tensile deformation could be due to the higher initial density of defects prior to deformation.

The microstructures after tensile deformation for the SMGT-aged-30 m sample are characterized and displayed in Figs. 11 and 12. As indicated in Fig. 11, non-planar dislocations and SFs are observed at both the topmost and the center layers, and the densities of defects are both high at these two positions. It is interesting to note that Lomer-Cottrell (L-C) locks are also formed at both the topmost and the center layers. The dislocations, SFs and L-C locks can all contribute significantly to the strain hardening for the SMGT-aged-30 m sample. The interactions between defects and $L1_2$ precipitates are revealed by bright-field and corresponding dark-field images at the topmost layer (Fig. 12a and b) and at the center layer (Fig. 12d and e), and also characterized by HRTEM images for the topmost layer (Fig. 12c) and the center layer (Fig. 12f). As indicated by dark-field images and HRTEM images, strong interactions between dislocations/SFs and $L1_2$ precipitates can be observed at both positions, resulting in strong precipitation hardening in the sample. Defects can be observed both in the interiors and at the outside of $L1_2$ precipitates, indicating a shearing precipitation hardening mechanism for $L1_2$ precipitates. The higher volume fraction and smaller spacing of $L1_2$ precipitates at the topmost layer can give rise to stronger precipitation hardening at the topmost layer, delaying the early strain localization at the topmost layer for better tensile ductility.

4. Concluding remarks

Heterogeneous structures with dual gradients of grain size and coherent $L1_2$ nanoprecipitation have been designed and fabricated in a $Co_{34.46}Cr_{32.12}Ni_{27.42}Al_3Ti_3$ MEA by SMGT and subsequent aging treatment. Then, the tensile properties and the corresponding deformation mechanisms of the structures with dual gradients have been investigated and compared with those of the single grain-size gradient structure and the coarse grained structures with homogeneously distributed $L1_2$ nanoprecipitates. The main concluding remarks are presented here.

(1) Synergy of yield strength and uniform elongation were observed to be improved in the structures with dual gradients, as compared to both the single grain-size gradient structure and the coarse grained structures with homogeneously distributed $L1_2$ nanoprecipitates.
(2) Structures with dual gradients show higher HDI hardening and stronger hardening capacities at each depth, as compared to the single grain-size gradient structure.
(3) Multiple deformation mechanisms, such as deformation twins and stacking faults, were both observed at both the topmost and center layers in the single grain-size gradient structure. However,

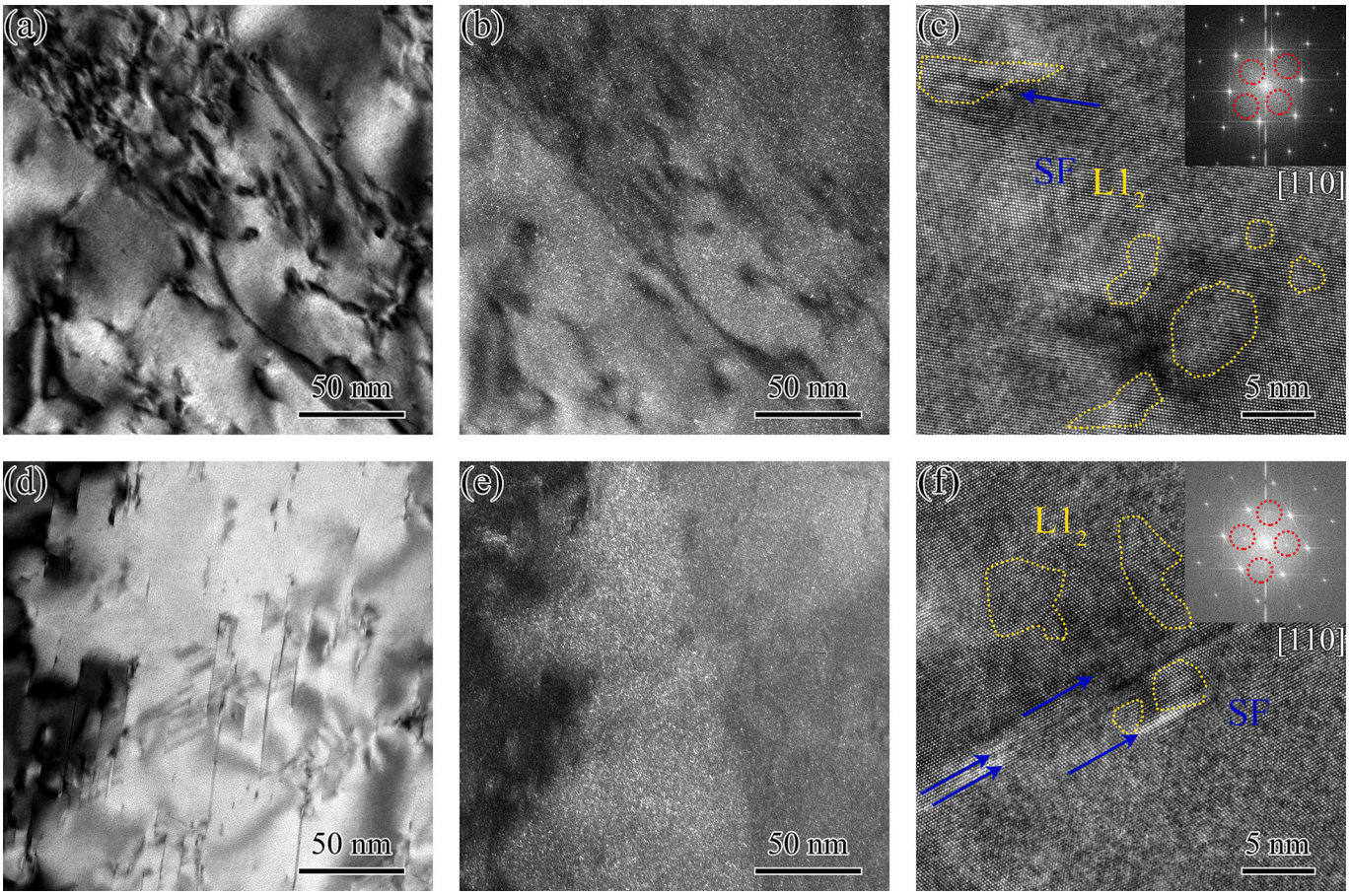

Fig. 12. TEM and HRTEM images for the SMGT-aged-30 m sample showing interactions between defects and $L1_2$ precipitates. (a) Bright-field TEM images at the topmost layer. (b) The corresponding dark-field image of (a), bright particles represent $L1_2$ precipitates. (c) HRTEM image at the topmost layer, indicating interactions between defects and $L1_2$ precipitates. (d) Bright-field TEM images at the center layer. (e) The corresponding dark-file image of (d), bright particles represent $L1_2$ precipitates. (f) HRTEM image at the center layer, showing interactions between defects and $L1_2$ precipitates.

deformation bands at two directions were only found at the topmost layer after tensile deformation in the single grain-size gradient structure. These formations of deformation bands at the topmost layer could be due to the severe plastic deformation magnitude during the SMGT process and the subsequent tensile deformation.

(4) Strong precipitation hardening at all depths can be achieved due to the interactions between defects and coherent $L1_2$ nanoprecipitates after tensile deformation in the structures with dual gradients. While, even stronger precipitation hardening can be induced at the topmost layer due to the higher volume fraction and smaller spacing of coherent $L1_2$ nanoprecipitates, which could retard the early strain localization trend at the topmost layer for better tensile properties in the structures with dual gradients. The present findings could provide the design strategy for achieving superior tensile properties in advanced metals and alloys.

Declaration of Competing Interest

The authors declare that they have no known conflict of interests in this paper.

Data availability

The raw/processed data required to reproduce these findings cannot be shared at this time due to technical or time limitations.

Acknowledgements

This research was supported by the NSFC Basic Science Center Program for “Multiscale Problems in Nonlinear Mechanics” [grant number 11988102], the National Key R&D Program of China [grant number 2019YFA0209902], and National Science Foundation of China [grant number 52192591].

References

[1] J.W. Yeh, S.K. Chen, S.J. Lin, J.Y. Gan, T.S. Chin, T.T. Shun, C.H. Tsau, S.Y. Chang, Nanostructured high-entropy alloys with multiple principal elements:novel alloy design concepts and outcomes, Adv. Eng. Mater. 6 (2004) 299–303.
[2] I. Gutierrez-Urrutia, D. Raabe, Influence of Al content and precipitation state on the mechanical behavior of austenitic high-Mn low-density steels, Scr. Mater. 68 (2013) 343–347.
[3] L.L. Zhu, C.S. Wen, C.Y. Gao, X. Guo, Z. Chen, J. Lu, Static and dynamic mechanical behaviors of gradient-nanotwinned stainless steel with a composite structure: experiments and modeling, Int. J. Plast. 114 (2019) 272–288.
[4] B. Gludovatz, A. Hohenwarter, D. Catoor, E.H. Chang, E.P. George, R.O. Ritchie, A fracture-resistant high-entropy alloy for cryogenic applications, Science. 345 (2014) 1153–1158.
[5] B. Schuh, F.M. Martin, B. Völker, E.P. George, H. Clemens, R. Pippan, A. Hohenwarter, Mechanical properties, microstructure and thermal stability of a nanocrystalline CoCrFeMnNi high-entropy alloy after severe plastic deformation, Acta Mater. 96 (2015) 258–268.
[6] X.L. Wu, Y.T. Zhu, Heterogeneous materials: a new class of materials with unprecedented mechanical properties, Mater. Res. Lett. 5 (2017) 527–532.
[7] E.P. George, D. Raabe, R.O. Ritchie, High-entropy alloys, Nat. Rev. Mater. 4 (2019) 515–534.
[8] L. Liu, Q.Yu.Z. Wang, J. Ell, M.X. Huang, Robert O. Ritchie, Making ultrastrong steel tough by grain-boundary delamination, Science 36 (2020) 1347–1352.

[9] R.Z. Valiev, Nanostructuring of metals by severe plastic deformation for advanced properties, Nat. Mater. 3 (2004) 511–516.
[10] Y.J. Liang, L.J. Wang, Y.R. Wen, B.Y. Cheng, Q.L. Wu, T.Q. Cao, Q. Xiao, Y.F. Xue, G. Sha, Y.D. Wang, Y. Ren, X.Y. Li, L. Wang, F.C. Wang, H.N. Cai, High-content ductile coherent nanoprecipitates achieve ultrastrong high-entropy alloys, Nat. Commun. 9 (2018) 4063.
[11] K.S. Ming, W.J. Lu, Z.M. Li, X.F. Bi, J. Wang, Amorphous bands induced by low temperature tension in a non-equiatomic CrMnFeCoNi alloy, Acta Mater. 188 (2020) 354–365.
[12] S.S. Sohn, A.K. Silva, Y. Ikeda, F. Kormann, W.J. Lu, W.S. Choi, B. Gault, D. Ponge, J. Neugebauer, D. Raabe, Ultrastrong medium-entropy single-phase alloys designed via severe lattice distortion, Adv. Mater. 31 (2019) 1807142.
[13] Q.F. Wu, F. He, J.J. Li, H.S. Kim, Z.J. Wang, J.C. Wang, Phase-selective recrystallization makes eutectic high-entropy alloys ultra-ductile, Nat. Commun. 13 (2022) 4697.
[14] M.A. Meyers, A. Mishra, D.J. Benson, Mechanical properties of nanocrystalline materials, Prog. Mater. Sci. 51 (2006) 427–556.
[15] M.X. Yang, D.S. Yan, F.P. Yuan, P. Jiang, E. Ma, X.L. Wu, Dynamically reinforced heterogeneous grain structure prolongs ductility in a medium-entropy alloy with gigapascal yield strength, P. Natl. Acad. Sci. USA. 115 (2018) 7224–7229.
[16] M.X. Yang, Y. Pan, F.P. Yuan, Y.T. Zhu, X.L. Wu, Back stress strengthening and strain hardening in gradient structure, Mater. Res. Lett. 4 (2016) 145–151.
[17] D. Choudhuri, B. Gwalani, S. Gorsse, M. Komarasamy, S.A. Mantri, S.G. Srinivasan, R.S. Mishra, R. Banerjee, Enhancing strength and strain hardenability via deformation twinning in fcc-based high entropy alloys reinforced with intermetallic compounds, Acta Mater. 165 (2019) 420–430.
[18] K.S. Ming, X.F. Bi, J. Wang, Realizing strength-ductility combination of coarse-grained Al0.2Co1.5CrFeNi1.5Ti0.3 alloy via nano-sized, coherent precipitates, Int. J. Plast. 100 (2018) 177–191.
[19] M. Singh, A. Das, T. Venugopalan, K. Mukherjee, M. Walunj, T. Nanda, B.R. Kumar, Impact of martensite spatial distribution on quasi-static and dynamic deformation behavior of dual-phase steel, Metall. Mater. Trans. A 49 (2017) 463–475.
[20] W. Moćko, A. Brodecki, L. Kruszka, Mechanical response of dual phase steel at quasi-static and dynamic tensile loadings after initial fatigue loading, Mech. Mater. 92 (2016) 18–27.
[21] T. Yang, Y.L. Zhao, J.H. Luan, B. Han, J. Wei, J.J. Kai, C.T. Liu, Nanoparticles-strengthened high-entropy alloys for cryogenic applications showing an exceptional strength-ductility synergy, Scr. Mater. 164 (2019) 30–35.
[22] Z.H. Zhang, P. Jiang, F.P. Yuan, X.L. Wu, Enhanced tensile properties by heterogeneous grain structures and coherent precipitates in a CoCrNi-based medium entropy alloy, Mater. Sci. Eng. A 832 (2022) 142440.
[23] H. Chang, T.W. Zhang, S.G. Ma, D. Zhao, T.X. Bai, K. Wang, Z.Q. Li, Z.H. Wang, Strengthening and strain hardening mechanisms in precipitation-hardened CrCoNi medium entropy alloys, J. Alloys Compd. 896 (2022) 162962.
[24] X.H. Du, W.P. Li, H.T. Chang, T. Yang, G.S. Duan, B.L. Wu, J.C. Huang, F.R. Chen, C.T. Liu, W.S. Chuang, Y. Lu, M.L. Sui, E.W. Huang, Dual heterogeneous structures lead to ultrahigh strength and uniform ductility in a co-Cr-Ni medium-entropy alloy, Nat. Commun. 11 (2020) 2390.
[25] J.Y. He, H. Wang, H.L. Huang, X.D. Xu, M.W. Chen, Y. Wu, X.J. Liu, T.G. Nieh, K. An, Z.P. Lu, A precipitation-hardened high-entropy alloy with outstanding tensile properties, Acta Mater. 102 (2016) 187–196.
[26] Z.G. Wang, W. Zhou, L.M. Fu, J.F. Wang, R.C. Luo, X.C. Han, B. Chen, X.D. Wang, Effect of coherent L12 nanoprecipitates on the tensile behavior of a fcc-based high-entropy alloy, Mater. Sci. Eng. A 696 (2017) 503–510.
[27] K. Lu, Nanomaterials. Making strong nanomaterials ductile with gradients, Science. 345 (2014) 1455–1456.
[28] X.D. Bian, F.P. Yuan, Y.T. Zhu, X.L. Wu, Gradient structure produces superior dynamic shear properties, Mater. Res. Lett. 5 (2017) 501–507.
[29] P.C. Zhao, B. Guan, Y.G. Tong, R.Z. Wang, X. Li, X.C. Zhang, S.T. Tu, A quasi-in-situ EBSD study of the thermal stability and grain growth mechanisms of CoCrNi medium entropy alloy with gradient-nanograined structure, J. Mater. Sci. Technol. 109 (2022) 54–63.
[30] T.H. Fang, W.L. Li, N.R. Tao, K. Lu, Revealing extraordinary intrinsic tensile plasticity in gradient Nano-grained copper, Science. 331 (2011) 1588–1590.
[31] X. Liu, F.P. Yuan, Y.T. Zhu, X.L. Wu, Extraordinary Bauschinger effect in gradient structured copper, Scr. Mater. 150 (2018) 57–60.
[32] X.L. Wu, M.X. Yang, F.P. Yuan, G.L. Wu, Y.J. Wei, X.X. Huang, Y.T. Zhu, Heterogeneous lamella structure unites ultrafine-grain strength with coarse-grain ductility, Proc. Natl. Acad. Sci. U. S. A. 112 (2015) 14501–14505.
[33] Y.T. Zhu, K. Ameyama, P.M. Anderson, I.J. Beyerlein, H.J. Gao, H.S. Kim, E. Lavernia, S. Mathaudhu, H. Mughrabi, R.O. Ritchie, N. Tsuji, X.U. Zhang, X. L. Wu, Heterostructured materials: superior properties from hetero-zone interaction, Mater. Res. Lett. 9 (2021) 1–31.
[34] X. Li, J. Zhang, D. Cui, X. Luo, H. Wang, Effects of Fe, Cr and Mn on inter-diffusion in CoNi-containing multiple principal alloys, Intermetallics. 140 (2022) 107400.
[35] Z. Li, S. Zhao, H. Diao, P.K. Liaw, M.A. Meyers, High-velocity deformation of Al0.3CoCrFeNi high-entropy alloy: Remarkable resistance to shear failure, Sci. Rep. 7 (2017) 42742.
[36] Z. Li, S. Zhao, S.M. Alotaibi, Y. Liu, B. Wang, M.A. Meyers, Adiabatic shear localization in the CrMnFeCoNi high-entropy alloy, Acta Mater. 151 (2018) 424–431.
[37] W.R. Jian, Z.C. Xie, S.Z. Xu, Y.Q. Su, X.H. Yao, I.J. Beyerlein, Effects of lattice distortion and chemical short-range order on the mechanisms of deformation in medium entropy alloy CoCrNi, Acta Mater. 199 (2020) 352–369.
[38] Y. Ma, F.P. Yuan, M.X. Yang, P. Jiang, E. Ma, X.L. Wu, Dynamic shear deformation of a CrCoNi medium-entropy alloy with heterogeneous grain structures, Acta Mater. 148 (2018) 407–418.
[39] S. Yoshida, T. Bhattacharjee, Y. Bai, N. Tsuji, Friction stress and Hall-Petch relationship in CoCrNi equi-atomic medium entropy alloy processed by severe plastic deformation and subsequent annealing, Scr. Mater. 134 (2017) 33–36.
[40] I. Moravcik, H. Hadraba, L.L. Li, I. Dlouhy, D. Raabe, Z.M. Li, Yield strength increase of a CoCrNi medium entropy alloy by interstitial nitrogen doping at maintained ductility, Scr. Mater. 178 (2020) 391–397.
[41] H. Chang, T.W. Zhang, S.G. Ma, D. Zhao, R.L. Xiong, T. Wang, Z.Q. Li, Z.H. Wang, Novel Si-added CrCoNi medium entropy alloys achieving the breakthrough of strength-ductility trade-off, Mater. Design. 197 (2021) 109202.
[42] C.E. Slone, J. Miao, E.P. George, M.J. Mills, Achieving ultra-high strength and ductility in equiatomic CrCoNi with partially recrystallized microstructures, Acta Mater. 165 (2019) 496–507.
[43] Z.H. Zhang, W. Wang, S. Qin, M. Yang, J. Wang Xin, P. Jiang, F.P. Yuan, X.L. Wu, Dual heterogeneous structured medium-entropy alloys showing a superior strength-ductility synergy at cryogenic temperature, J. Mater. Res. Tech 17 (2022) 3262–3276.
[44] S. Qin, M.X. Yang, P. Jiang, J. Wang, X.L. Wu, H. Zhou, F.P. Yuan, Designing structures with combined gradients of grain size and precipitation in high entropy alloys for simultaneous improvement of strength and ductility, Acta Mater. 230 (2022) 117847.
[45] X.L. Wu, M.X. Yang, R. Li, P. Jiang, F.P. Yuan, Y. Wang, Y.T. Zhu, Y.J. Wei, Plastic accommodation during tensile deformation of gradient structure, Sci. China Mater. 64 (2021) 1534–1544.
[46] S. Qin, M.X. Yang, P. Jiang, F. Yuan, X. Wu, Excellent tensile properties induced by heterogeneous grain structure and dual nanoprecipitates in high entropy alloys, Mater. Charact. 186 (2022) 111779.
[47] C.W. Yang, X.L. Jiang, W.Q. Zhang, X.L. Wang, Enhancing stress corrosion cracking resistance of machined surface via surface mechanical grinding treatment for AISI 316 L stainless steel, Mater. Charact. 194 (2022) 112493.
[48] Y.F. Wu, Y.M. Zhong, W. Xu, X.Y. Li, Deformation induced grain boundary segregation and thermal stability of nanolaminated Al-Zn-Mg-Cu alloy, Mater. Lett. 315 (2022) 131930.
[49] K. Rambabu, P. Gandhi, M. Susmitha, K. Sravanthi, A review on different techniques to produce gradient structured material, Mater. Today. Proc. 60 (2022) 2262–2265.
[50] W. Zhang, M.C. Zhao, Z. Wang, L. Tan, Y. Qi, D.F. Yin, K. Yang, A. Atrens, Enhanced initial biodegradation resistance of the biomedical mg-cu alloy by surface nanomodification, J. Magnes. Alloy. 5 (2022) 7–26.
[51] X. Chen, F. Yuan, H. Zhou, X. Wu, Structure motif of chemical short-range order in a medium-entropy alloy, Mater. Res. Lett. 10 (2022) 149–155.
[52] X. Liu, H. Feng, J. Wang, X. Chen, P. Jiang, F. Yuan, H. Li, E. Ma, X. Wu, Mechanical property comparisons between CrCoNi medium-entropy alloy and 316 stainless steels, J. Mater. Sci. Technol. 108 (2022) 256–269.
[53] J. Wang, P. Jiang, F. Yuan, X. Wu, Chemical medium-range order in a medium-entropy alloy, Nat. Commun. 13 (2022) 1021.